Evaluation of Steady-State, Time- and Frequency-Domain Data for the Problem of Optical Diffusion Tomography

H. L. Graber, R. L. Barbour[†], and J. Lubowsky
Departments of Pathology and Biophysics, SUNY Health Science Center at Brooklyn,
450 Clarkson Ave., Brooklyn, NY 11203

R. Aronson
Department of Physics, Polytechnic University,
333 Jay St. Brooklyn, NY 11201

B. B. Das, K. M. Yoo, and R. R. Alfano
Institute of Ultrafast Spectroscopy and Lasers, Department of Electrical Engineering and Physics,
City College of the City University of New York, NY, NY 10031

[†]Author to whom inquiries should be addressed.

Abstract

The three techniques of CW, time-gated and frequency modulation measurements are examined and compared for their ability to provide clues to the macroscopic optical properties of multilayer random media. For each illumination scheme, a simple algorithm is described which is capable of identifying important parameters such as the ratio of macroscopic absorption cross-sections across layer boundaries, and the depth of boundaries in two- and three-layer media. The algorithms are developed by consideration of data from Monte Carlo simulations, and in the case of the time- and frequency-domains are tested by using them to analyze experimental data.

1.0 Background

This paper deals with one aspect of a concerted research program for the development of methods for imaging the interior of a highly scattering medium[1-4]. The intended application of these studies is to develop a practical imaging scheme which is capable of yielding 3-D optical images of tissue based on measurements performed at near infrared frequencies (700-1300 nm). For most of our work to date, we have modeled photon transport in tissue using a diffusion-based particle model with elastic scattering. Most recently, we have begun to consider more advanced schemes which include the refraction and reflection of light at internal boundaries[4]. Previously, we have reported partial solutions to the problem of imaging in highly scattering media[5-8]. There are two efforts being pursued in parallel[2,3]. Both iteratively modify the current estimate until the detector readings calculated for the reconstructed medium match the measured readings. They differ in their approaches for obtaining the forward solution, i.e., calculating the detector readings and their gradients for the current estimate, and for the inverse update, i.e., modifying the estimate to reduce the difference between the calculated and detected readings. The first approach has made extensive use of Monte Carlo methods in the forward solution calculations[5,7]. The updated inverse is obtained by solving a linear perturbation equation[3]. The second approach uses a neural network scheme to solve the inverse problem[2,8]. The forward solution is obtained by a relaxation method, which essentially solves the differential equation corresponding to the transport equation. The inverse update is accomplished by a least-mean-squares learning algorithm.

Both methods call for caution in their implementation. The difficulty lies in the uncertainty of the paths of the detected signals, which makes the inverse problem inherently underdetermined. Without the use of sufficient *a priori* information other than the raw detector readings, a solution may be found which is mathematically correct but physically inaccurate. Both methods thus require some assistance to be successfully implemented.

Our approach to addressing this need has been to consider strategies which provide reliable *a priori* information about the structure, or at least limits on the range of possible structures, that the object under study may possess. This is accomplished by "preprocessing" the raw data predominantly using heuristically derived methods which are computationally non-intensive.

In addition to recognizing the importance of identifying and making use of *a priori* constraints, it has become apparent that for any practical imaging scheme, considerations of computation time and computational complexity are paramount and unavoidable. This issue, as a general problem, is an area one of us (F. Schlereth) has examined closely. It has led to the development of a novel approach for evaluating ultra-large scale computing problems, of which the problem of imaging in diffusing media is an example, and is considered more fully in reference 2.

2.0 Introduction

In this paper, we begin our consideration of the problem of imaging in diffusing media by examining the three different illumination schemes which have been employed for studying the optical properties of tissue[9]. These are CW or time-independent[10], time-gated[11,12], and frequency-modulated[13] measurements. The aim of this report has been to explore the development of strategies which evaluate the different illumination schemes and yield elementary qualitative information on the range of permissible values for a medium's optical properties from simple, computationally unintensive, treatments of the raw detector responses. We consider these schemes because of our belief that, for many practical problems, the inverse problem will be ill-posed and will, therefore, require use of *a priori* information to constrain the range of permissible results. The type of media we considered are those in which radiation transport occurs predominantly by a diffusion process. Because our focus here was to develop methods which could aid in image recovery, attention was paid to how well posed the "inversion scheme" was. We refer to these treatments as "data preprocessing," and they are intended to discover the presence of boundaries between layers with different optical properties by determining the approximate depths at which the boundaries occur and the approximate degree of change in absorption cross-section from one layer to the next. In a related study, we previously demonstrated, using time-independent data[14], that information of this type could be identified if the responses of coupled pairs of detectors were examined.

For each of the illumination schemes mentioned, our approach has been to examine signals which exit the same surface that they entered through. This has the practical advantage that the measurement can be truly remote, with no need to place the specimen, or patient, inside the measuring device. Time-independent measurements offer the advantage of having high signal-to-noise ratios while requiring the least sophistication of instrumentation design, cost, and operator skill. Time-gated measurements add an additional degree of freedom for the reconstruction problem but require instrumentation of much greater complexity and cost and require greater skill on the part of the operator. Somewhat in between are frequency modulated schemes, in which the intensity of the source is varied sinusoidally with time about a mean DC level[15]. A detector located some distance away on the surface will detect an oscillating signal having the same frequency. The ratio of the AC amplitude to the DC level and the phase of the detected signal have been shown to be sensitive to the presence of heterogeneities in the medium[13] in a frequency-dependent manner. Thus, relative to the time independent case, this scheme also affords additional degrees of freedom. Frequency modulated measurements may also provide the practical advantage of having higher signal-to-noise ratios when compared to time-gated signals, especially at low frequencies which propagate deeply into the target medium; however, this likely comes at the expense of reduced spatial resolution.

3.0 Methods

3.1 Computing Facilities

Source codes for the Monte Carlo simulations were written in standard Fortran 77 language and implemented on a newly developed four-node parallel multicomputer, called Kilonode (see third paper in this series for description) which is attached to the 'Cat' SUN network at Syracuse University. Because of its high speed and efficiency (320 Mflops), use of Kilonode permitted the simulation of media using source conditions and detector configurations which previously would not have been feasible due to the inefficiency of scoring tightly collimated receivers, as well as to the added computational requirement for resolving the temporal profile of detector responses. Despite these added requirements, simulations involving 40-70 million photon histories, averaging 30 collisions per history, could be completed within one CPU day.

3.2 Monte Carlo Simulations

All media modeled in this study were half-spaces in which the total cross-section, Σ_t, was held constant at a value of 1.0 MFP^{-1} (MFP = mean free pathlength). This required that incremental changes in the absorption cross-section, Σ_a, were compensated for by adjusting the scattering cross-section, Σ_s, to maintain their sum, Σ_t, a constant. Two different source conditions were modeled, time-independent and time-resolved. In both, the source was directed normally to the surface, and backscattered photons were detected by tightly collimated receivers located at increasing radial distances from the source. Each simulation modeled 15 sets of detectors, accepting photons emerging from the medium at distances in the range of n - 0.5 to n + 0.5 MFP, n = 1,2,...15. Within every set were nine detectors, each accepting photons emerging within a small solid angle (~.095 sr) about its central axis. The detector geometry was a circular cone having an acceptance angle of 10° about the central axis. A total of nine detector axes were arranged at inclination angles ranging from $\emptyset = 0°$ to $\emptyset = 80°$ in 10° steps, and all were set at an azimuthal angle, Φ, of 0°; i.e. the axes of the source and detector axes intersect inside the medium.

Techniques used to maximize the efficiency of the simulations included treating each photon as an ensemble, with a variable weight that was decreased upon each collision to account for the probabilities of absorption and escape from the medium. When the weight fell below 0.2, a Russian roulette routine was invoked. Basing each decision on a number sampled from a random variable with a uniform distribution, the photon history was terminated in 80% of the cases, and, as a compensating measure, the weight was increased by a factor of 5 the remaining 20% of the time. Photon histories were terminated only by Russian roulette; the function from which the free-flight distance was selected after each collision was renormalized to prevent the photons from being lost through the boundary. Scoring was performed on collisions in which the direction of scattering was towards the boundary. Its path was extrapolated to the point at which it intersected the boundary, and if it lay within the acceptance cone of a detector, the detector's score was incremented. The increment was the product of the photon's weight after the scattering and the probability of a photon propagating from the collision site to the detector without having another collision. Correlated sampling, in which photons were forced to follow identical paths in the test and reference media but with weights adjusted separately, was employed to minimize the sampling error between the two media. All intensities and associated standard errors were reported in units of no. photons detected/ incident photon/ sr / MFP^2.

Simulations of the detector responses for time-resolved studies were performed in the same manner as that described above, with the modification that detected photons were binned according to the total distance they had propagated in the medium. Each time window contained photons exiting the medium after propagating a total distance between n and n + 1 MFP, n = 0,1,...99.

3.3 Calculation of Fourier Transforms of Time-Domain Data

Frequency-domain data was obtained by calculating the discrete Fourier transform (FT) of simulated and experimental data. To reduce noise in the experimental data, a 9-point moving average was computed prior to performing the FT calculation. In addition, each smoothed profile was compared to the original profile before the FT calculation, to ensure that the smoothing procedure had not artifactually distorted the shape or height of the peak. For experimental data, approximately 400 data points, spanning a time window of 0-1500 ps, were used to calculate the transform. Because of lower noise levels in the simulated data, smoothing was not required. Extrapolations out to 1600 MFP were made by performing regression analysis on the linear portion (30-60 data points) of the log I vs. time plot in order to eliminate the artifact that would result from a non-zero difference between the initial and final data points, and to reduce the interval between successive frequencies in the transforms.

3.4 Solutions to the Time-Dependent Diffusion Equation

The "method of images," with the assumption that diffuse light intensity falls to zero at the boundary, was used[16] to calculate the intensity in a half-space medium. Fick's law, $J = -D\nabla\Phi$, which relates flux and intensity, gives the following expression for the flux at the surface, where r is the distance from the source, all photons are assumed to have their first collisions at a depth z_1 below the surface, c is the speed of light in the medium, D is the diffusion coefficient, and t is time:

$$ J = |J_z| = \frac{1}{8} \frac{1}{\sqrt{(\pi Dc)^3 t^5}} exp\left(-\frac{r^2 + z_1^2}{4Dct}\right) exp(-\Sigma_a ct) \quad (\equiv J_{\text{point}}) \tag{1}$$

A more realistic model for the source condition for the case of a medium illuminated by a narrow collimated beam is that every point on the ray $r = r_0$ is a source point, with the source strength decreasing exponentially with increasing depth; $s = \Sigma_s exp(-\Sigma_t z_1)\delta(r - r_0)\delta(t - t_0)$. The corresponding diffuse flux is the integral from $z_1 = 0$ to $z_1 = \infty$ of the product of the source condition and the single-point flux:

$$ J = \int_0^\infty s J_{\text{point}} dz_1 \quad (\equiv J_{\text{ray}})$$

$$ = \frac{1}{8} \frac{\Sigma_s}{\sqrt{(\pi Dc)^3 t^5}} exp\left(-\frac{r^2}{4Dct} - \Sigma_a ct\right) \int_0^\infty z_1 exp\left(-\frac{z_1^2}{4Dct} - \Sigma_t z_1\right) dz_1 \tag{2}$$

While this integral could be approximated by a finite sum of discrete source points, it is possible to evaluate the integral analytically and use the analytical solution. The solution is:

$$ J = \frac{1}{4} \frac{\Sigma_s}{\sqrt{Dc(\pi t)^3}} exp\left(-\frac{r^2}{4Dct} - \Sigma_a ct\right)\left[1 - \Sigma_t\sqrt{\pi Dct} \, exp(\Sigma_t^2 Dct) \, erfc\left(\Sigma_t\sqrt{Dct}\right)\right] \tag{3}$$

Once the source condition is extended in the z-direction, however, it should take into account the fact that a finite time must elapse between the pulse entering the medium $(t = t_0)$ and the first scatterings that occur at depth z_1 $(t = t_0 + z_1 c^{-1})$; $s = \Sigma_s exp(-\Sigma_t z_1)\delta(r - r_0)\delta(t - t_0 - \frac{z_1}{c})$ is the expression for this source condition. The integral in eq. (2) can be evaluated between any finite limits z_l and z_h; the result is:

$$J(z_l, z_h, t) = \frac{1}{4} \frac{\Sigma_s}{\sqrt{Dc(\pi t)^3}} exp\left(-\frac{r^2}{4Dct} - \Sigma_a ct\right) \cdot \tag{4}$$

$$\cdot \left[exp\left(-\frac{z_l^2}{4Dct} - \Sigma_t z_l\right) - exp\left(-\frac{z_h^2}{4Dct} - \Sigma_t z_h\right) - \Sigma_t \sqrt{\pi Dct}\, exp(\Sigma_t^2 Dct) \cdot \right.$$

$$\left. \cdot \left(erf\left(\frac{z_h + 2\Sigma_t Dct}{2\sqrt{Dct}}\right) - erf\left(\frac{z_l + 2\Sigma_t Dct}{2\sqrt{Dct}}\right)\right)\right]$$

When weighted by the source strength function, the mean value of z in the interval from z_l to z_h is:

$$\overline{z_{l,h}} = \frac{1}{\Sigma_t} + \frac{z_l exp(-\Sigma_t z_l) - z_h exp(-\Sigma_t z_h)}{exp(-\Sigma_t z_l) - exp(-\Sigma_t z_h)} \tag{5}$$

The diffuse flux for this source condition can then be numerically evaluated as:

$$J = \lim_{(z_{n+1}-z_n)\to 0} \sum_{n=0}^{\infty} J\left(z_n, z_{n+1}, t - \frac{\overline{z_{n,n+1}}}{c}\right) \tag{6}$$

where $z_o = 0$ and $J(z_l, z_h, t) = 0$ when t<0.

3.5 Experimental Studies

Ultrafast laser pulses were generated from a home-built colliding pulse mode-locked (CPM) dye laser pumped by a Spectra Physics 171 Argon laser. The laser pulses at 620 nm had an output power of 5 mW, a repetition rate of 82 MHz and a pulse duration of 100 fs. The main beam was focused into a 100 μm diameter multimode fiber by a micro-objective lens (model no. M20X, Newport) and this fiber delivered the ultrafast pulses into a cylindrical tank (20 cm diameter and 12 cm depth) filled with a random scattering medium. The scattering medium was prepared by diluting whole milk (Delwood Co.) with water to 25% concentration. The backscattered pulse at various distances r (2.5 to 12.5 mm in steps of 2.5mm) from the point of incidence was collected by another fiber and delivered to the streak camera (C1587 Hamamatsu Co.). The fibers were placed about 0.5 mm above the surface of the medium. Small portions of the laser beam were split off for triggering the streak camera and for a reference pulse to establish a zero-value for time. The temporal profile of the scattered pulse was measured by the synchroscan streak camera. An aluminum sphere of 10 mm diameter and with a matte black finish was used as the absorber. The effect of this ball on the backscattered pulse was studied. An illustration of the experimental set-up is shown below in Sketch 1.
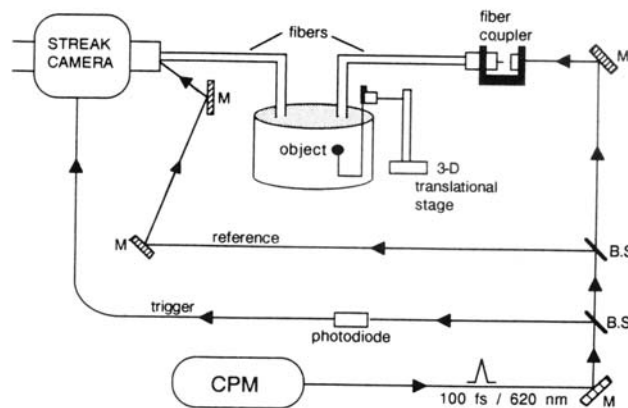
Legend to sketch 1: the experimental set-up. M = mirror, B.S. = beam-splitter.

The transport mean free path and the absorption length of the medium were measured using the transmission technique described in Yoo et al[17]. The values obtained were 0.82 mm and 253 mm, respectively.

4.0 Results

4.1 Evaluation of Time-Independent Data

An example of the difficulty encountered when attempting to deduce subsurface structure from inspection of raw data is shown in Figure 1A. The three curves shown are plots of intensity vs. distance for time-independent signals, obtained by Monte Carlo simulation, for a homogeneous half-space and two different layered media. The curves shown are monotonic and lack features which would readily identify the presence or characteristics of an heterogeneity. The gross features of the layered media are revealed, however, if a comparison is made between a reference and test medium by computing the ratio of responses of pairs of detectors positioned a fixed distance apart. In the example shown in Fig. 1B, the thickness of the intermediate layer was varied. The plotted function would always have a value of 1.0 if the test and reference medium were identical. The function values become greater than 1.0 if the second layer has a higher absorption cross-section than the first, and less than 1.0 if the absorption of the deeper layer is smaller. While the curve approaches a constant value different from 1.0 in the limiting case in which the second layer is a half-space, it reaches a maximum and then moves back toward values of 1.0 if the second layer has a finite thickness.

Previously[14], we performed a similar analysis on results obtained from simulated studies in which either the depth or contrast of the intermediate layer was varied. The results contained features which readily distinguished the effect of increasing the depth of the intermediate layer from that of diminishing the contrast
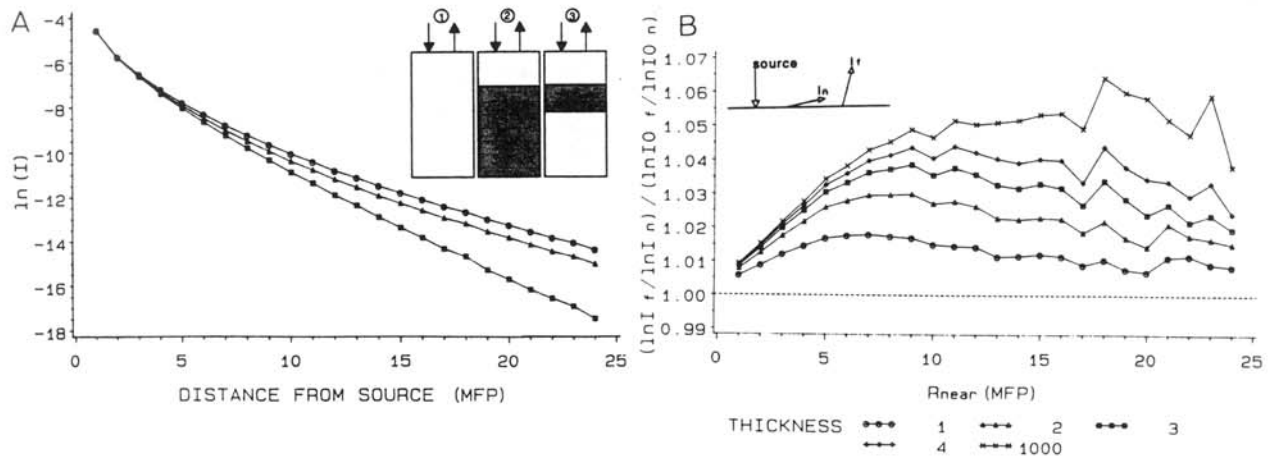

Legend to Figure 1: Panel A. Results shown were obtained by simulating the responses of conical detectors having an acceptance angle of 10° and orientated 10° from vertical, at the indicated distance, with source and detector axes coplanar. Medium 1 (O - O): homogeneous half-space, $\Sigma_a/\Sigma_t = .01$; Medium 2 (□-□): two layers, top layer Σ_a/Σ_t (thickness (MFP)) = .01(3), bottom layer = .05(∞); Medium 3 (Δ - Δ): three layers, first layer = .01(3), second layer = .05(1), bottom layer = .01(∞). Panel B. Plots of calculated ratios of logarithms of intensities of coupled pairs of detectors. I_n and $I0_n$ are intensities measured by detectors closer to the source (n = "near"), I_f and $I0_f$ are intensities measured by detectors farther from the source (f = "far"). $I0_n$ and $I0_f$ are intensities of light reflected from reference medium, I_n and I_f are intensities of light reflected from layered media. The orientation and configuration of the detectors is the same as in Panel A except I_n detectors had a grazing orientation 80°

from vertical. The distance separating the detector pairs was 1.0 MFP. The reference medium is a homogeneous half-space with the same Σ_a/Σ_t and Σ_t as the first layer of the stratified medium. First layer Σ_a/Σ_t (thickness (MFP)) = .01(3); second layer = .05 (m), m = 1-4, ∞; third layer = .01(∞)
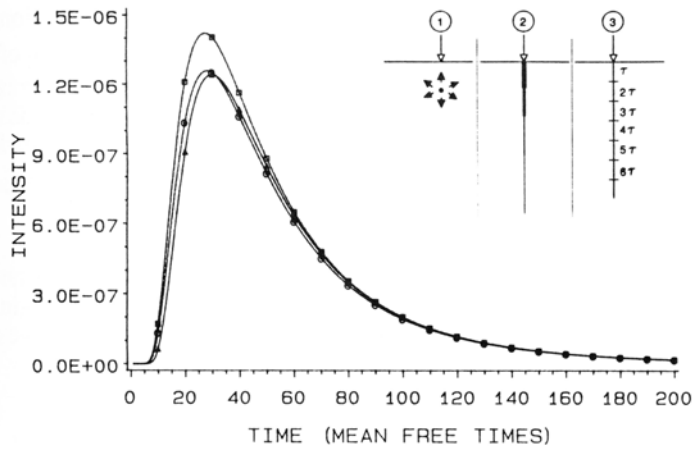
between the two layers.

4.2 Evaluation of Time-Domain Data

Many studies appearing in recent years have emphasized the advantages that data obtained from time- and frequency-domain measurements have over those from continuous-wave measurements. Since the goal of this study was to identify procedures for more easily deducing subsurface structure, we next focused our attention on examining these alternative measurement schemes. Results in Figure 2A were obtained by simulating time-gated measurements of the same three media described in Figure 1. The detector configuration was also the same as in Figure 1 and located 5 MFP from the source. Figure 2B shows results of experimental measurements in which a 5-mm radius black sphere was submerged in diluted whole milk with its center 10 mm below the surface, a depth at which it was not visible from the surface by eye. While it is evident that the temporal profiles shown in the Figure are influenced by the presence of subsurface structures, inversion to reveal elementary characteristics of these structures cannot be made from a casual inspection of the data.
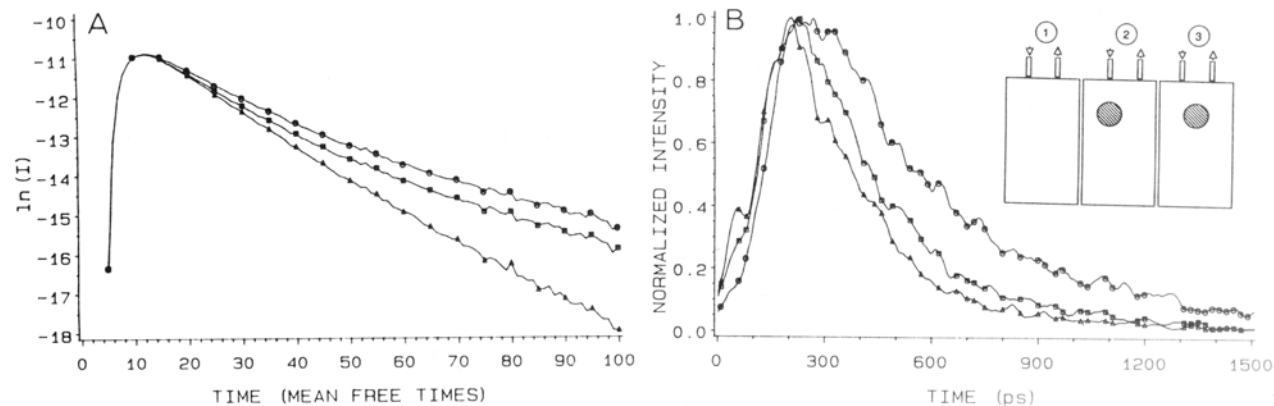
Legend to Figure 2: Intensity vs. time profiles of backscattered photons from simulated and experimental media. Mean free time (MFT) = time required for a photon to move a distance of 1 MFP. Panel A. Media examined have the same composition as in Figure 1A: (O - O), homogeneous medium; ($\square$-$\square$), two layer medium; (Δ - Δ), three layer medium. Panel B. Media are milk-water mixtures (see Methods); target is a black bead. (O - O), bead is not present; ($\square$-$\square$), bead center directly under source fiber; (Δ - Δ), bead center displaced 5 mm from source fiber in the direction of the detector fiber, line joining source and detector bisects absorber. In this and subsequent figures, symbols for individual data points are included for ease of distinguishing different curves, and only a small fraction of data points are explicitly indicated.

An analytical approach to estimating the properties of a target medium would be to obtain a best fit of the solution of the time-dependent diffusion equation to the experimental data, as was suggested by Patterson et al[12]. Results in Figure 3 show solutions to this equation, for three different source conditions, for a homogeneous half-space. The source conditions examined correspond to successively more realistic approximations to the distribution of first collisions in a scattering medium. The first approximation, which is most commonly used, is that all photons will experience their first collision at a depth exactly 1 MFP below the surface. The second approximation is that the first collision occurs on a straight line on which the source strength decreases exponentially with increasing depth. The third approximation is similar to the second, but takes into account that there is a time delay, directly proportional to the depth, for first collisions. A comparison of the results shown demonstrate that the greatest differences between the three solutions occur at early times and they converge at longer times.

One would expect that the third case could best approximate measured data. Our experience has been that although somewhat better fits to the temporal profiles were obtained using the last approximation, in many cases they were not too dissimilar from the other source conditions modeled. More important was the observation that even though relatively good fits to the temporal profiles could be obtained, they were not unique. Model parameter estimates anywhere in a 2-to-3-fold range often fit a given profile equally well. In other cases (i.e., certain orientations for collimated detectors), the diffusion solutions were quite evidently poor models for the shape of the temporal profiles and the regression procedures failed to converge. In view of the non-uniqueness of the calculated parameters with homogeneous media, it is suspect whether this type of analysis could reliably deduce the properties of more complex layered media, especially when effects such as refraction and internal reflection at the boundary are incorporated in the boundary conditions.

Examination of the forms of the diffusion solutions did suggest an alternative way of evaluating the temporal profiles. The solutions for all three source conditions are alike in that the effect of homogeneous absorption can be factored out; the solution for a medium with homogeneous absorption is simply the product of that for a nonabsorbing medium and an exponential term, with the decay constant equal to the product of the Σ_a and c. Thus if a comparison is made between two media which differ only in degree of absorption, using the same source-detector configuration, all factors other than the exponential will cancel when the ratio of intensities are calculated as a function of time. The logarithm of the intensity ratio, plotted against time, would be a straight line whose slope is the product of c and the difference between Σ_a of the two media[††]. When this relationship was tested using data from Monte Carlo simulations of homogeneous half-space media, excellent agreement (<5% error) with the expected result from the diffusion solution was observed. Moreover, this agreement was independent of the degree of detector collimation, source-detector separation and detector orientation. The greatest deviations from linearity observed were at early times, where validity of the diffusion approximation is poorest.

This behavior suggests a simple method for discovering the desired information about a layered medium. Plots of ln(I/I$_{ref}$), where I is the temporal profile from a multilayer medium and I$_{ref}$ is the corresponding profile from a homogeneous reference medium, should deviate from linearity in a characteristic manner depending on the properties of the test medium. Examples of this are shown in Figure 4. The curves in Fig. 4A are derived from two-layer media in which the thickness of the first layer is varied (1-5 MFP) while the absorption contrast is held constant (1%:5%). The time t_o corresponds to the minimum time needed for light

---

[††] It is recognized that if all other cross-sections and the scattering anisotropy factor are held constant, the diffusion coefficient will change as Σ_a is varied. In the simulation studies discussed here, Σ_s was adjusted also so that Σ_t (and hence D) would be constant. Even if this had not been the case, the variation in D would not have been significant, as Σ_a << (1-g)Σ_s.

to travel the (fixed) distance from source to detector. The additional time required (t_1-t_5) before deviation from zero is observed corresponds to the amount of time which must pass before light can reach the depth of the boundary and return to the detector $(t \geq c^{-1}(r^2 + 4z^2)^{1/2}$, where r is the source-detector separation and z is the depth of the boundary). The negative slopes of the curves immediately indicates that the second layer has a higher Σ_a than the first, while the fact that the curves approach a linear asymptote indicates that the second layer is a half-space. The limiting slope reached is the same in all cases, indicating that $(\Sigma_a-\Sigma_a\text{ref})$ is constant.

The results shown in Fig. 4B are also derived from two-layered media. Here the thickness of the first layer is held constant (3 MFP) and the absorption contrast varied (1%: 2-10%). In this case, all curves begin to differ from zero at the same value of t_1 as would be expected. As the deep layer is a half-space, all curves are asymptotic to straight lines whose limiting slope are proportional to $\Sigma_a-\Sigma_a\text{ref}$.
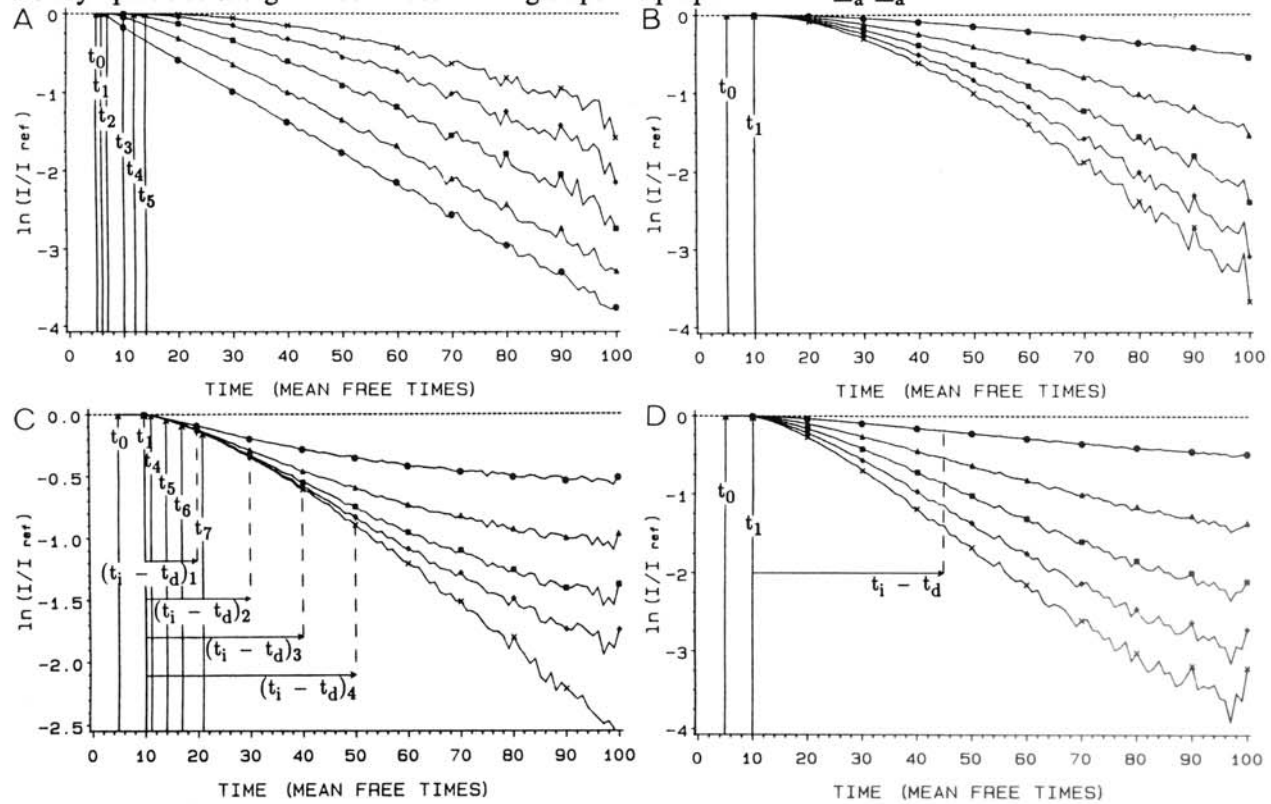

Legend to Figure 4: $\ln(I/I_{ref})$ vs. t, at r = 5 and $\emptyset = 10°$, for four sets of multilayer media. The reference medium in every case is a homogeneous half-space, with $\Sigma_a = .01\Sigma_t$. Panel A: test media have two layers; first layer Σ_a (thickness (MFP)) = .01(n), n = 1,2,...,5, second layer = .05 (∞); t_o is time delay between incident pulse and initial detector response, t_n is time at which $\ln(I/I_{ref})$ first becomes <0; $t_o = 5$, $t_1 = 6$, $t_2 = 7$, $t_3 = 10$, $t_4 = 12$, $t_5 = 14$. Panel B: test media have two layers; first layer = .01(4), second layer = k(∞), k = .02, .04, ..., .1; $t_o = 5$, $t_1 = 10$. Panel C: test media have three layers; first layer = .01(3), second layer = .05(n), n = 1,2,3,4,∞, third layer = .01(∞); $t_o = 5$, $t_1 = 10$, t_m, m = 4-7, is time at which curve for deep boundary at m diverges from curve for two-layer limiting case; $t_4 = 11$, $t_5 = 14$, $t_6 = 17$, $t_7 = 21$; $t_d = t_1$, $t_{i1} = 20$, $t_{i2} = 30$, $t_{i3} = 40$, $t_{i4} = 50$. Panel D: test media have three layers; first layer = .01 (3), second layer = k(4), k = .02, .04, ..., .1, third layer = .01(∞); $t_o = 5$, $t_1 = 10$; $t_d = t_1$, $t_i = 45$. Symbols used in A and C: n=1, (O - O); n=2, (Δ - Δ); n=3, ($\square$-$\square$); n=4, ($\lozenge$ - $\lozenge$); n=5 (A) or n=∞ (C), (x - x). Symbols used in B and D: k=.02, (O - O); k=.04, (Δ - Δ); k=.06, ($\square$-$\square$); k=.08, ($\lozenge$ - $\lozenge$); k=.10, (x - x).

Qualitatively different behavior is obtained in the graphs of $\ln(I/I_{ref})$ when the second layer is an inclusion of finite thickness. Fig. 4C shows results in which the interlayer absorption contrast and first boundary depth were fixed (1%:5% and 3 MFP respectively), and the thickness of the darker layer was varied (1-4, ∞ MFP). The limiting case of an infinitely thick second layer produces a result of the same type as seen in Fig. 4A. Because the first boundary is fixed, all curves begin to differ from zero at the same value of t, as seen in Fig. 4B. When the second layer is finite, however, $\ln(I/I_{ref})$ eventually diverges from the curve for the two-layer limiting case, and the absolute value of the slope decreases. Because Σ_a of the third layer is the same as in the first, it is expected that at longer times the slope will approach zero. The value of t at which this divergence occurs is a function of the deeper boundary depth (same functional form as above). This in itself does not yield a practical scheme for estimating the thickness of the layer, as the limiting curve will not, in general, be known. However, inspection of the derivatives of the curve reveals that the quantity $(t_i - t_d)$ is directly proportional to the thickness of the intermediate layer, where t_i is the time at which the inflection (maximum slope) occurs and t_d is the time at which the curve begins to differ from zero (results not shown).

Results shown in Fig. 4D are the converse of those in Fig. 4C. Here the thickness (4MFP) and depth (located between 4-7 MFP) of middle layer is fixed and the contrast is varied (1%:2-10%). As in the case in Fig. 4C, the slope is expected to approach zero as t increases. All curves in this set have their inflection points at the same value of t, consistent with the observation above that the quantity is dependent on the thickness of the second layer.

While the type of information illustrated in Figure 4 could serve a useful function in constraining the image-reconstruction problem, consideration of the likely noise levels which would be encountered in plots of experimental data are of concern. Examination of the experimental results shown in Figure 5 demonstrate, however, that a great deal of *a priori* information suitable for use in image recovery is present. The four curves shown are plots of $\ln(I/Iref)$ vs. t for four different locations of the source fiber relative to the absorber, with the detector fiber 2.5 mm from the source in each case. While it is not possible to attempt to identify inflection points or limiting slopes, two clear trends are present. The major trend distinguishes the cases in which the absorber lies entirely on one side of the source-detector axis from those in which the axis bisects the absorber. The smaller trend within each set is related to the minimum distance light must travel from the source fiber to the absorber and back to the detector fiber. From these data and the previously noted relationships between the rate of deviation from zero and the boundary depth and contrast (see Figure 4A and 4B), it can be inferred that the medium contains a heterogeneity more strongly absorbing than the surroundings, and which appears limited in lateral extent and whose depth varies beneath different points on the surface. This latter conclusion is strengthened by the apparent deviation from zero of the curve corresponding to source location 1 at a slightly earlier time than that for the other sources.
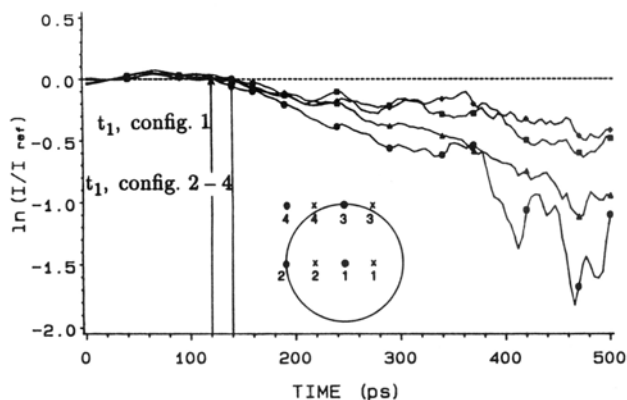

Legend to Figure 5: $\ln(I/I_{ref})$ vs. t for experimental data, r = 2.5 mm. Four curves correspond to different source-detector configurations. Configuration 1 (O - O): source fiber over center of absorber; configuration 2 (Δ - Δ), source fiber over edge of absorber, source-detector axis bisects absorber; configuration 3 ($\square$ - $\square$), source fiber over edge of absorber, source-detector axis rotated 90° with respect to configuration 2; configuration 4 ($\Diamond$ - $\Diamond$), detector fiber over absorber edge, source-detector axis the same as in configuration 3. t_1 = 120 ps for config. 1, 140 ps for config. 2-4. Inset shows the four configurations in a plane parallel to the medium's surface. Dots indicate source fiber locations, crosses the detector fiber locations.

4.3 Evaluation of Frequency Domain Data

For reasons previously mentioned, it was also desirable to examine frequency-domain data. Calculation of frequency-domain results were obtained by determining the Fourier transforms of calculated and measured temporal profiles. An example of the output for simulated data is shown in Figure 6. The data shown here were obtained from homogeneous media with different values of Σ_a. The amplitudes of the transforms were normalized to the value of the DC component for the medium having the smallest Σ_a, and are shown in Fig. 6A. The amplitude decreases rapidly with increasing frequency, as must be the case when a function and its derivative both are everywhere continuous. As Σ_a increases, the width of the temporal profile decreases, and the FWHM of the amplitude vs. frequency plot increases as expected.

The phase portion of the transforms are shown in Fig. 6B. Each curve is qualitatively similar to that which would be obtained for a simple decaying exponential function; the curve is asymptotic to a straight line whose slope is proportional to the time delay between a pulse entering the medium and the beginning of the detector response.

In order to gain insight into the structure of the media, it is more useful to calculate the ratio of the Fourier amplitudes of the test and reference media and the difference between their phases, as a function of the modulation frequency. Results shown in Fig. 6C and 6D illustrate this calculation for the data presented in Fig. 6A and 6B, with the medium having the lowest value of Σ_a serving as the reference. Inspection of the Figure reveals that the amplitude ratio levels off to a constant value as frequency increases and that the limiting values are functions of the $\Sigma_a/\Sigma_a\text{ref}$. The important observation here is that the amplitude ratio stabilizes at values different from 1.0 and the phase differences approach values different from zero.
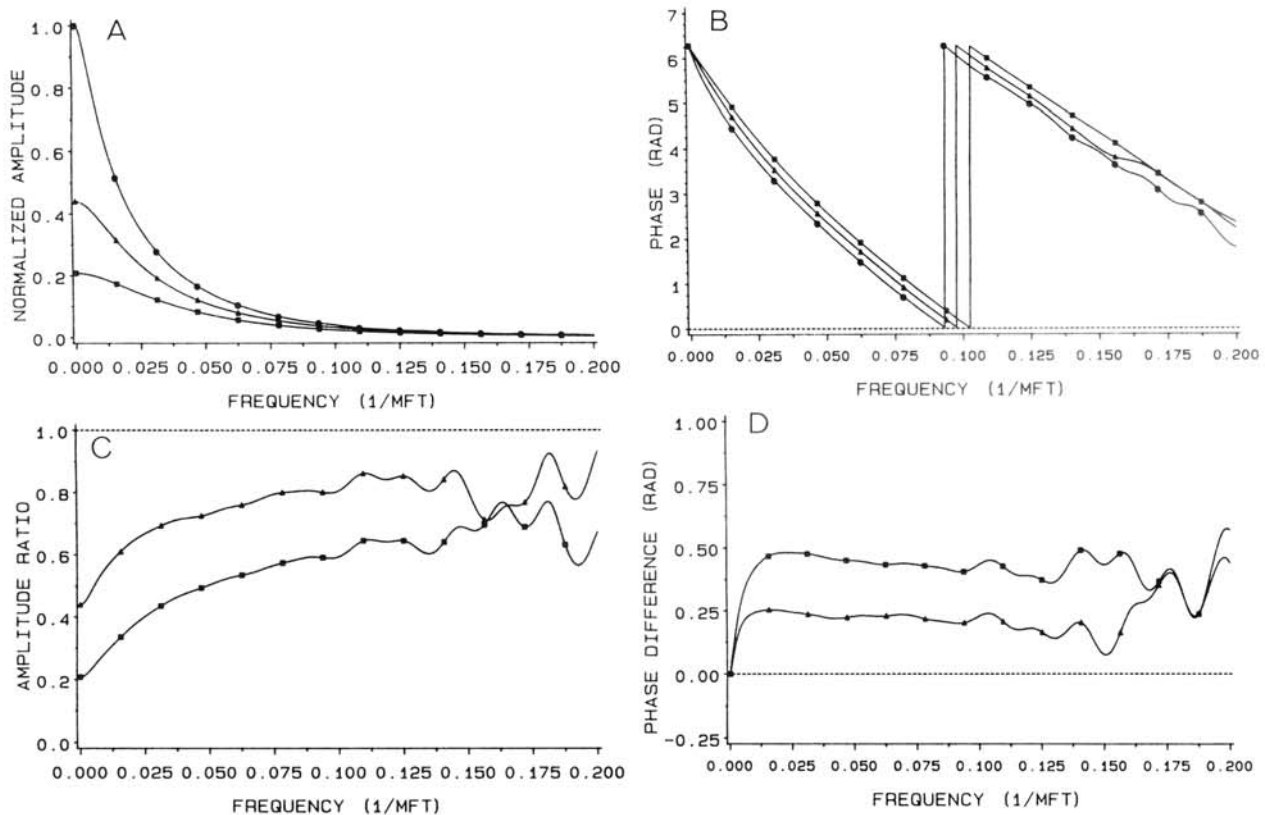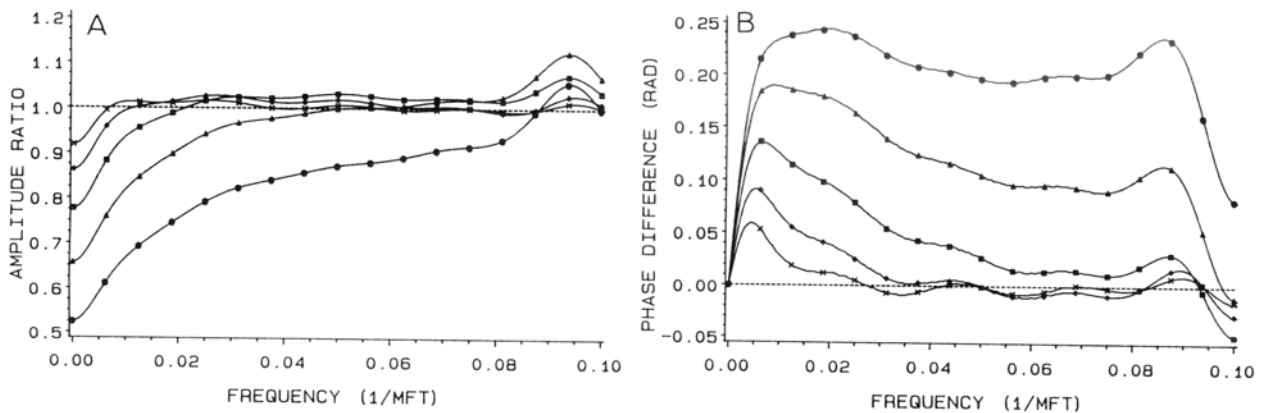
Legend to Figure 6: Discrete Fourier transforms of temporal profiles from simulations. Media are homogeneous half-spaces, $\Sigma_t = 1.0$, $r = 5$, $\emptyset = 0°$. (O - O), $\Sigma_a = .01$; (Δ - Δ), $\Sigma_a = .05$; ($\square$-$\square$), $\Sigma_a = .1$. Panel A: amplitude of FT's vs. modulation frequency relative to DC component for case of $\Sigma_a = .01$. Panel B: phases of FT's vs. modulation frequency; discontinuity is "wrap-around" that occurs due to restriction of phases to the interval 0-2π. Panel C: amplitude ratios vs. modulation frequency; (Δ - Δ), ampl. ($\Sigma_a = .05$)/ ampl. ($\Sigma_a = .01$); ($\square$-$\square$), ampl. ($\Sigma_a = .1$)/ ampl.($\Sigma_a = .01$). Panel D: phase difference vs. modulation frequency; (Δ - Δ), phase ($\Sigma_a = .05$) - phase ($\Sigma_a = .01$); ($\square$-$\square$), phase ($\Sigma_a = .1$) - phase ($\Sigma_a = .01$).
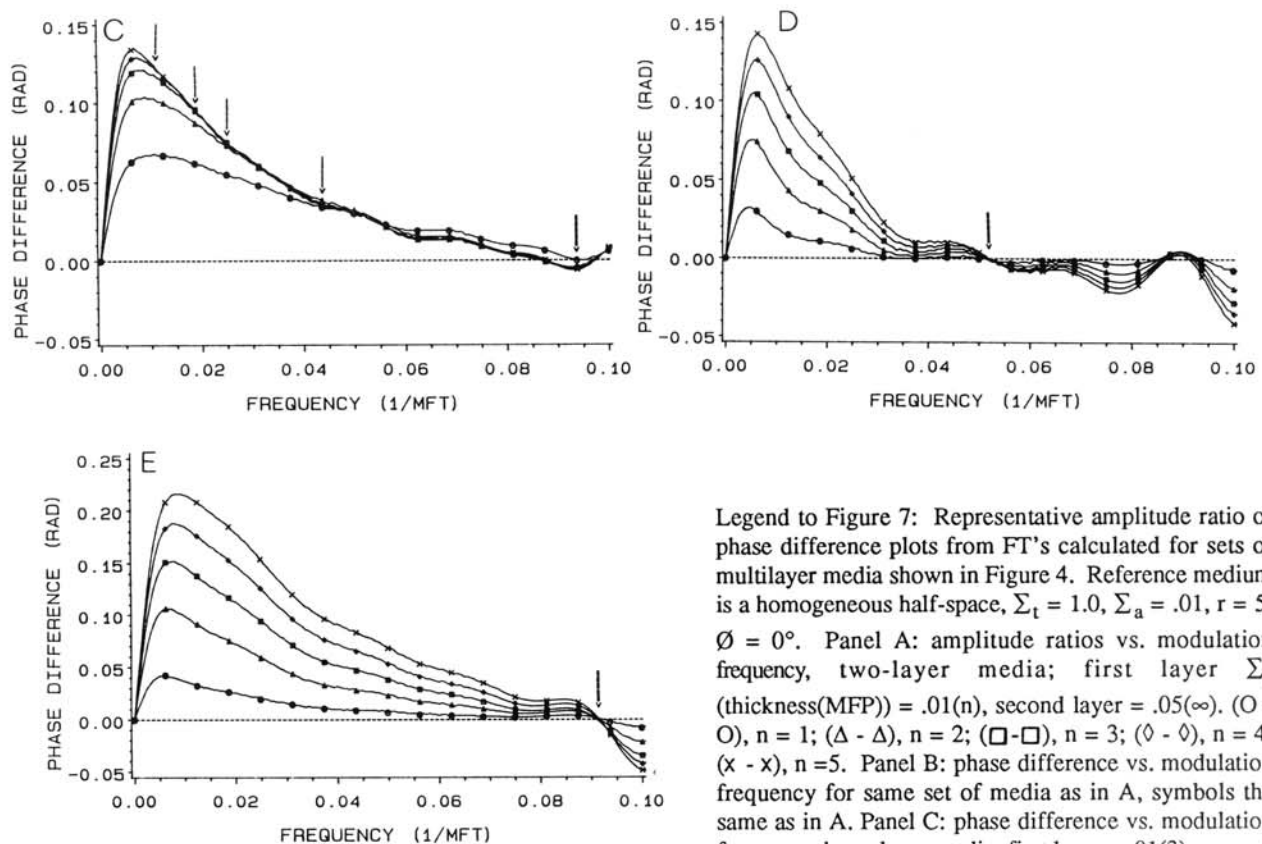
As was discussed by Fishkin et. al.[13], when light from a sinusoidally varying source is introduced into a scattering medium, the oscillations are rapidly damped out as the photon density waves propagate outward. There is a maximum depth below which the light intensity will not vary in time, at which point the intensity will be the same as if a time-independent source had been used. This maximum depth is frequency dependent and decreases as the modulation frequency increases. As a consequence of this relationship, it would be expected that if two media are identical up to a certain depth and differ thereafter, a critical frequency can be found below which a divergence in a plot of amplitude ratio or phase difference will occur, and the point of departure will be proportional to the depth of the boundary.

This expectation is borne out by examining the data presented in Figure 7A and 7B. The data shown represent the transforms of data in Figure 4 A and B. The amplitude ratio is initially less than 1.0 in all cases, and remains so to a high frequency when the boundary is 1 MFP below the surface, but as the boundary depth increases the highest frequency at which the ratio differs from 1.0 rapidly falls. The same trend is seen in the phase difference, which falls to zero at a frequency which decreases as the depth of the boundary increases.

Fig. 7C shows the phase difference plots for the same set of three-layer media whose time-domain results are shown in Figure 4C. Here all curves fall to zero at about the same frequency, which is consistent with the fact that the first interlayer boundary is at the same depth in all five cases. Information about the deeper boundary would be obtained, if at all, at lower frequencies. Here it is seen that, as expected from the discussion above, the highest frequency at which the phase difference diverges from that for the two-layer limiting case rapidly decreases as the thickness of the intermediate layer increases. In the absence of the curve for the limiting case it is difficult to estimate the thickness of the layer from the shape of the curve. Evidently there is a relationship between the maximum phase difference and the frequency at which convergence to the two-layer limiting case is observed, but it is not a simple linear relation such as described earlier for the time-domain data.

Fig. 7D and 7E show the phase difference plots for the same sets of two- and three-layer media for which the time-domain data were presented in Figure 4B and 4D. In each case the curves all fall to zero at about the same frequency, indicating the first boundary occurs at the same depth. This frequency is lower for the

Panel C — PHASE DIFFERENCE (RAD) vs FREQUENCY (1/MFT)

Panel D — PHASE DIFFERENCE (RAD) vs FREQUENCY (1/MFT)

**Panel E** — PHASE DIFFERENCE (RAD) vs FREQUENCY (1/MFT)

Legend to Figure 7: Representative amplitude ratio or phase difference plots from FT's calculated for sets of multilayer media shown in Figure 4. Reference medium is a homogeneous half-space, $\Sigma_t = 1.0$, $\Sigma_a = .01$, $r = 5$, $\emptyset = 0°$. Panel A: amplitude ratios vs. modulation frequency, two-layer media; first layer Σ_a (thickness(MFP)) = .01(n), second layer = .05(∞). (O - O), n = 1; (Δ - Δ), n = 2; ($\square$-$\square$), n = 3; ($\Diamond$ - $\Diamond$), n = 4; (x - x), n =5. Panel B: phase difference vs. modulation frequency for same set of media as in A, symbols the same as in A. Panel C: phase difference vs. modulation frequency, three -layer media; first layer = .01(3), second layer = .05(n), n = 1,2,3,4,∞, third layer = .01(∞). (O - O), n =1; (Δ - Δ), n =2; ($\square$-$\square$), n = 3; ($\Diamond$ - $\Diamond$), n = 4;(x - x), n = ∞. Panel D: phase difference vs. modulation frequency, two-layer media; first layer = .01(4), second layer = k(∞), k = .02, .04, ..., .1. (O - O), k = .02; (Δ - Δ), k = .04; ($\square$-$\square$), k = .06; ($\Diamond$ - $\Diamond$), k = .08; (x - x), n = .10. Panel E: phase difference vs. modulation frequency, three-layer media; first layer = .01(3), second layer = k(4), k = .02, .04, ..., .1, third layer = .01(∞); symbols same as in D. Double-shafted arrows in panels C, D, and E point to frequency indicative of the depth of the shallow boundary. Single-shafted arrows in panel C point to frequencies indicative of the depth of the deep boundary (see text for analysis).

curves in Fig. 6D, as expected, because the boundary is deeper for this set of media. There is, unfortunately, no feature at the lower frequencies, when comparing the two panels or when comparing the corresponding amplitude plots (not shown), that permits one to identify if the thickness of the second layer is finite.

In spite of this incomplete success in deducing the structure of a medium from these simple examinations of the frequency-domain data, useful information can be extracted from an examination of the Fourier transforms of the experimental data shown in Figure 5. In this case the desired information is more easily obtained by examining plots of the amplitudes and amplitude ratios as a function of the modulation frequency. The inset to Figure 8A shows the four locations of source and detector fibers corresponding to four of the curves; the fifth (solid) curve is the amplitude in the absorberless reference case. There are two trends seen in the data in both Fig. 8A and Fig. 8B. As was the case in Figure 5, the larger trend is related to movement of the source-detector axis towards the edge of the absorber, and the smaller trend to the position of the source and detector along their axis. In Fig. 8B it is seen also the the amplitude ratio curves for the source-detector axis bisecting the absorber remain at values less than 1.0 to a higher frequency than those for the absorber lying to one side of the axis. This is consistent with a conclusion that the depth of the absorber is less when the fibers are in these positions, i.e. that it has a curved surface.
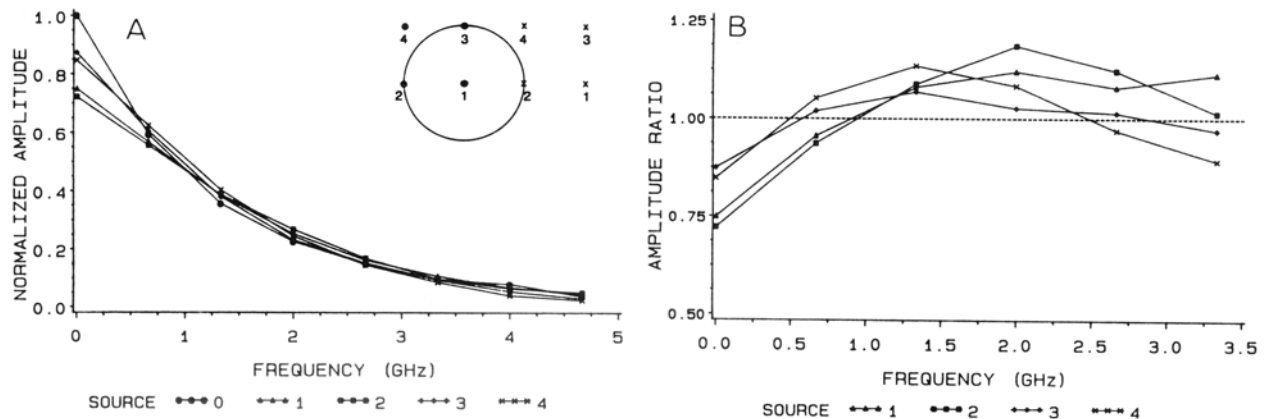
Legend to Figure 8: FT's of experimental time-domain data, R = 10 mm. Panel A: Fourier amplitudes vs. modulation frequency. (O - O), reference medium, absorber not present; see Legend of Figure 5 for description of source-detector configurations. (Δ - Δ), config., 1; (□-□), config., 2; (◊ - ◊), config., 3; (x - x), config., 4. Panel B: amplitude ratio vs. modulation frequency. (Δ - Δ), config. 1/ref.; (□-□), config. 2/ref.; (◊ - ◊), config. 3/ref.; (x - x), config. 4/ref.

5.0 Discussion and Future Directions

As explained above, it is often desirable to derive as much *a priori* information as possible about the permissible ranges of values in different regions of an unknown medium before attempting image reconstruction. It has been shown here how this information can be obtained from reflectance measurement data, using simple analyses which do not require knowledge of the theoretical form that the detector response function should have, for any of the three most extensively studied illumination schemes. While is appears on the basis of the data presented here that each technique has limitations, trends in the data support the optimistic view that these are the result of limitations in the quantity and quality of the data we have examined.

In the case of continuous illumination, the function plotted in Figure 1B suffers from the drawback that the ordinate axis is not scale-invariant, and requires careful detector calibration for its implementation. When the ordinate axis is plotted as simply the double ratio of intensities, rather than the double ratio of their logarithms, qualitative information related to the structure of the medium is also apparent in the plot. Further, the former plot has the desirable feature of ordinate scale invariance. In the limited number of plots examined using this approach, however, the degree and rate of change of the function and its derivative were not as great as seen in Figure 1B, rendering interpretation more difficult.

Our analysis of time-domain data is mathematically simpler than that for the CW case, is scale-invariant, and does not require comparison of the responses of two detector readings of the test medium. These advantages alone, however, would not justify implementing a time-gated measurement scheme. There are advantages to using time-gated data in image reconstruction[1], and it has been shown here how the *a priori* information that the various algorithms call for[2,3] may readily be obtained from these data. It may appear from Figure 5 that although qualitative inferences can be drawn from examination of real data, the sort of quantitative analysis described in the presentation of Figure 4 is precluded by poor signal-to-noise ratios. It should be noted, however, that the signal-to-noise ratio present in the data considered above was far from optimal. Improvements in the optical coupling between laser and source fiber, as well as employing different gain settings on the streak-camera in different portions of the temporal profile, should significantly improve the quality of the data.

The treatment of frequency-domain data that was presented in Figure 7 showed that in at least one case it was not possible to obtain information, the thickness of the dark second layer, which was apparent in the

time-domain data presented in Figure 4 (4C vs. 4A, and 4D vs. 4B). However, the data in Figure 7 were obtained indirectly, by calculating the FT's of time-domain data, and the presence of noise in the latter greatly restricts the range of frequencies that can be accurately represented. This, and the small number of distinct cases available for study, restrict conclusions concerning whether the apparent limitation shown here is real. It is always possible that more sophisticated techniques will be developed which will reveal the missing structural features, or that the acquisition of a more complete and accurate set of data will show it actually is present in the analysis presented above. Given that time- and frequency-domain measurements are related by being a Fourier pair, there is a theoretical reason to expect that any information present in one should also be present in the other. On the other hand, since probing to greater depths requires the use of lower modulation frequencies with concomitant loss of spatial resolution, there is also reason to believe that the presence of the deep boundary may be invisible to the frequency-domain technique.

6.0 References

[1] R.L. Barbour, H.L. Graber, J. Lubowsky, R. Aronson, B.B. Das, K.M. Yoo, and R.R. Alfano, "Imaging of Diffusing Media by a Progressive Iterative Backprojection Method Using Time-Domain Data," SPIE, vol 1641, accompanying paper in these proceedings, 1992.

[2] F.H. Schlereth, J. M. Fossaceca, A.D. Keckler and R.L. Barbour, " Imaging of Diffusing Media with a Neural Net Formulation: a Problem in Large-Scale Computation," SPIE, vol 1641, accompanying paper in these proceedings, 1992.

[3] Y. Wang, J.H. Chang, R. Aronson, R.L. Barbour, H.L. Graber and J. Lubowsky, "Imaging in Random Media by Diffusion Tomography: An Iterative Perturbation Approach," SPIE,vol 1641, accompanying paper in these proceedings, 1992.

[4] R. Aronson, "Exact Interface Conditions for Photon Diffusion," SPIE, vol 1641, accompanying paper in these proceedings, 1992.

[5] R.L. Barbour, H.L. Graber, R. Aronson, and J. Lubowsky, "Model for 3-D Optical Imaging of Tissues," Proceedings of 10th Annual International Geoscience and Remote Sensing Symposium (IGARSS), vol 2, pp 1395-1399, 1990.

[6] R. Aronson, R. L. Barbour, J. Lubowsky and H. Graber, "Application of Transport Theory to NIR Medical Imaging," *Modern Mathematical Models in Transport Theory; Advances and Applications*, vol 51, pp 64-75, Birkhauser Press, 1991.

[7] R.L. Barbour, H.L. Graber, R. Aronson and J. Lubowsky, "Imaging of Subsurface Regions of Random Media by Remote Sensing," SPIE vol 1431, pp 192-203, 1991.

[8] F.H. Schlereth, J. M. Fossaceca, A.D. Keckler and R.L. Barbour, "Multicomputer-based Neural Networks for Imaging in Random Media," IEEE Nucl. Sci. Symp., Sante Fe, NM, *in press*, November 1991.

[9] B. Chance, "Optical Method," Ann. Rev. Biophys. Biophys. Chem, 20, pp 1-28, 1991.

[10] K.M. Yoo, G.C. Tang, R.R. Alfano, "Coherent backscattering of light from biological tissues," Appl. Opt., 29, pp 3237-3239, 1990.

[11] K.M. Yoo, R.R. Alfano, "Determination of the scattering and absorption lengths from the temporal profile of a backscattered pulse," Opt. Lett., 15, pp 276-278, 1990.

[12] M.S. Patterson, B. Chance, B.C. Wilson, "Time resolved reflectance and transmittance for the noninvasive measurement of tissue optical properties", Appl. Opt., 28, pp 2331-2336, 1989.

[13] J. Fishkin, E. Gratton, M.J. van de Ven, W.W. Mantulin, "Diffusion of Intensity Modulated Near-Infrared Light in Turbid Media," SPIE, vol 1431, 122-135, 1991.

[14] R.L. Barbour, H.L. Graber, R. Aronson and J. Lubowsky, "Determination of Macroscopic Optical Properties of Multilayer Random Media by Remote Sensing," SPIE vol 1431, p 52-62, 1991.

[15] E.M. Sevick, B. Chance, J. Leigh, S. Nioka, and M. Maris, "Quantitation of Time- and Frequency-Resolved Optical Spectra for the Determination of Tissue Oxygenation," Anal. Biochem., 195, 330-351, 1991.

[16] J. R. LaMarsh, *Introduction to Nuclear Reactor Theory*, chap. 5, Addison Wesley, Publishing Co., NY, 1966.

[17] K.M. Yoo, F. Liu, R.R. Alfano, "When Does the Diffusion Approximation Fail to Describe Photon Transport in Random Media?" Phys. Rev. Lett., 64, pp 2647-2650, 1990. Erratum: *op. cit.*, 65, p 2210, 1990.